

Reconciliation of contrasting theories for fracture spacing in layered rocks

Martin P.J. Schöpfer*, Arzu Arslan†, John J. Walsh, Conrad Childs

*Fault Analysis Group, UCD School of Geological Sciences,
University College Dublin, Belfield, Dublin 4, Ireland.*

Abstract

Natural and man-made brittle layers embedded in a weaker matrix and subjected to layer-parallel extension typically develop an array of opening-mode fractures with a remarkably regular spacing. This spacing often scales with layer thickness, and it decreases as extension increases until fracture saturation is reached. Existing analytical one-dimensional (1-D) 'full-slip' models which assume that interfacial slip occurs over the entire length of the fracture-bound blocks predict that the ratio of fracture spacing to layer thickness at saturation is proportional to the ratio of layer tensile to interface shear strength (T/τ). Using 2-D discontinuum mechanical models run for conditions appropriate to layered rocks we show that the validity and consequent applicability of these 1-D models depends on T/τ . High T/τ ratios (*ca.* > 3.0) promote interfacial slip and yield results that, in terms of fracturing and interfacial slip evolution, provide a good fit to a 1-D shear lag model, which, in the limit, becomes the 'full-slip' model. At lower T/τ ratios, however, interfacial slip is suppressed and the heterogeneous 2-D stress distribution within fracture-bound blocks controls further fracture nucleation. Our models suggest that 1-D approximations for predicting the spacing of fractures in layered materials are erroneous for low T/τ ratios.

Keywords: Fracture spacing; Rock joints; Shear lag model; Distinct Element Method;

*Corresponding author. E-mail: martin@fag.ucd.ie Tel: +353 1 716 2611 Fax: +353 1 716 2607

†Present address: Center for Marine Environmental Sciences, Leobener Strasse, D-28359 Bremen, Germany.

1 Introduction

Opening-mode fractures are extremely common phenomena in natural and man-made materials. In geosciences they are referred to as joints (Mandl, 2005) and in engineering they are termed cracks (Nairn, 2000). In mechanically layered materials, such as sedimentary rock sequences or laminates, these fractures typically form perpendicular to the layer boundaries and are often best, or exclusively, developed in the stiffer and more brittle layers (Fig. 1a), although under some circumstances fractures may first form in the weaker beds (Bourne, 2003). Studies of these fractures in layered rocks (Ladeira and Price, 1981, Huang and Angelier, 1989, Narr and Suppe, 1991, Ji and Saruwatari, 1998, Ji et al., 1998, Gillespie et al., 2001, Iyer and Podladchikov, 2009), physical experiments (Garrett and Bailey, 1977, Mandal et al., 1994, Wu and Pollard, 1995) and numerical models (Tang et al., 2008) have revealed that fracture spacing increases with layer thickness. A wide variety of mechanisms have been suggested for the origin and scaling relations of layer-confined opening-mode fractures (Bourne, 2003, Mandl, 2005). In the present study, we focus on one of the most commonly used boundary conditions for investigating the mechanics of opening-mode fractures in layered materials: fracturing due to layer-parallel extension under constant layer normal stress. For this case, experimental work has revealed that fracture spacing decreases approximately as the inverse of the applied layer-parallel strain (Manders et al., 1983, Parvizi and Bailey, 1978). This is because new fractures form in-between existing fractures, a process referred to as *sequential infilling* (Bai et al., 2000, Bai and Pollard, 2000b). Eventually no new fractures form, irrespective of any further increase in applied strain, a condition called *fracture saturation* (Wu and Pollard, 1995, Bai et al., 2000, Bai and Pollard, 2000b, Dharani et al., 2003).

The earliest and most commonly invoked mechanical explanation for fracture saturation is that the fracture spacing reaches a critical value (relative to the layer thickness, t) at which maximum tensile stresses within the fracture bound blocks are too low to yield further fracture. This explanation is based on the concept of frictional coupling between the fractured layer and the ambient material or 'matrix' (Fig. 1b). The layer/matrix

29 interface has a frictional strength τ given by the Coulomb limit stress $\sigma_n\mu$, where σ_n is
 30 the interfacial normal stress and μ is the interfacial friction coefficient (Mandl, 2005). The
 31 static balance of mechanical forces requires that a constant interfacial shear stress, τ , is
 32 balanced by a constant layer-parallel *average* stress gradient, $d\sigma_x/dx$ (Fig. 1b). If slip
 33 occurs over the entire length of a fracture-bound block (*full-slip* conditions), the layer-
 34 parallel normal stress (σ_x) distribution between two traction free fractures is triangular,
 35 with the maximum tensile stress occurring in the block centre (Fig. 1b). This central
 36 maximum tensile stress is, however, limited by the tensile strength of the layer, T . The
 37 *critical fracture spacing* (s_c) is therefore defined as the spacing below which the maximum
 38 tensile stress can not reach the layer strength, i.e. $s_c = Tt/\tau$ (Fig. 1b).

39 The above equation is known as Price's model in the geologic literature (Price, 1966,
 40 Mandl, 2005) and as the Kelly-Tyson equation in material sciences (Kelly and Tyson,
 41 1965, Tripathi and Jones, 1998). For laminates and fibre composites, it is widely applied
 42 to estimate interfacial shear strength from fragment length measurements (Tripathi and
 43 Jones, 1998). This *full-slip* model is the most commonly applied end-member of a suite of
 44 models referred to as *shear lag models* (Cox, 1952, Hobbs, 1967, Piggott, 1978, Lloyd et al.,
 45 1982, Berthelot et al., 1996, Ji and Saruwatari, 1998, Ji et al., 1998, Berthelot, 2003, Jain
 46 et al., 2007). Different shear lag models vary in the assumed modes of transfer of tensile
 47 stress across the layer/matrix interface, e.g. the full-slip model is the limit solution (at
 48 infinite layer extension; $e \rightarrow \infty$) for a cohesionless frictional interface. Although differing
 49 in detail, shear lag models all predict that sequential infill fractures should form midway
 50 between existing fractures, such that the range of fracture spacing at a particular strain
 51 varies by a factor of two, i.e. $0.5s_c, < s < s_c$. The average fracture spacing is hence given
 52 by $\bar{s} = 0.75s_c$, an expression sometimes referred to as the Ohsawa *et al.* equation (Ohsawa
 53 et al., 1978, Tripathi and Jones, 1998).

54 Despite their successful application in material science (Berthelot et al., 1996, Berthelot,
 55 2003), the limitations of shear lag models are manifest in a variety of ways. For
 56 example, whilst physical experiments without any clear evidence for interfacial slip can

67 attain fracture saturation (Garrett and Bailey, 1977), shear lag models with inhibited in-
68 terfacial slip ($\tau \rightarrow \infty$) predict fracturing *ad infinitum* (Bai et al., 2000). In addition, they
69 are unable to account for fracture clustering in 'corridors' (Olson, 2004) or 'crack families'
60 (Groves et al., 1987) and for the formation of splay, i.e. branch, fractures. This is because
61 the feature common to all shear lag models is that they are based on stresses averaged
62 over the thickness of the layer, i.e. they are effectively 1-D treatments. Consideration of
63 layer-normal σ_{xx} variations and the near crack tip stress field on fracturing is thus absent.

64 **Figure 1**

65 An alternative explanation for fracture saturation in the absence of interfacial slip
66 is that segment-bounding fractures become sufficiently closely spaced such that a layer-
67 parallel compressive normal stress arising between the existing fractures prevents the
68 insertion of new fractures (Altus and Ishai, 1986). This is referred to as *compressive*
69 *stress criterion* (CSC; Dharani et al., 2003) or *stress-transition theory* (Bai et al., 2000,
70 Bai and Pollard, 2000b). The CSC is based on 2-D numerical (Bai et al., 2000, Bai and
71 Pollard, 2000b, Korach and Keer, 2002, Li and Yang, 2007) and analytical (Schoep-
72 ner and Pagano, 1999, Adda-Bedia and Amar, 2001) modelling of the stress distribution
73 between two predefined fractures. For a fracture spacing to layer thickness ratio of ap-
74 proximately one, this modelling reveals that a region of compressive layer-parallel normal
75 stress σ_{xx} develops right across the central area of the fracture-bound block (Bai et al.,
76 2000, Bai and Pollard, 2000b, Fig. 1c). This central compression belt will inhibit further
77 fracturing, although numerical analysis indicates that tensile stresses adjacent to the in-
78 terface (Fig. 1c) may be sufficient to cause propagation of vertical fractures across this
79 belt from interface-flaws mid-way between the two existing fractures (Bai and Pollard,
80 2000a). Fracture saturation occurs when a limiting fracture spacing to thickness ratio is
81 reached, at which fractures can not propagate across the compressive belt. For identical
82 layer and matrix elastic properties, this limit is $s/t = 0.546$, such that s_{min}/t for a fracture
83 set at complete infilling would be 0.273 (Bai and Pollard, 2000a). This predicted range is
84 referred to as the *2-D infill criterion*.

85 Whilst the CSC theory provides a rationale for fracture saturation without interfacial
86 slip, unlike the shear lag models, it is limited because it does not include such slip. Exper-
87 imental studies on fibres (Huang and Young, 1995, van den Heuvel et al., 1997, Tripathi
88 and Jones, 1998) and laminates (Berthelot, 2003), for example, have shown that during
89 extension interfacial slip, or, in the presence of cohesion, interface debonding, occurs.
90 Analysis of plume lines on joint faces also suggests that interfacial, e.g. bedding parallel,
91 slip or matrix yielding must sometimes occur during joint growth (Savalli and Engelder,
92 2005). Moreover, and importantly, the CSC theory does not account for observations of
93 fracture saturation at s/t ratios in excess of one.

94 The above considerations suggest that a fuller explanation of fracture scaling relation-
95 ships for the wide range of naturally occurring and man-made interface properties requires
96 a more complete model definition, ideally one which incorporates behaviours explained by
97 both theories illustrated in Fig. 1. Here we describe discontinuum numerical models that
98 explicitly replicate fracturing of a layer in response to layer-parallel extension and to 2-D
99 stress distributions within fracture blocks. We consider a range of layer/matrix interface
100 properties and compare our model results with those of shear lag and CSC theories.

101 **2 Methods**

102 *2.1 Model geometry and boundary conditions*

103 In our discontinuum models the layer and matrix are represented as an assemblage of
104 bonded circular particles (Fig. 2; Potyondy and Cundall, 2004). The bonds between
105 particles comprising the central layer fail if their strength is exceeded and the linkage of
106 those broken bonds leads to the formation of fractures. The particles and bonds do not
107 represent sand grains and cement, respectively; they merely provide a numerical material
108 that mimics the mechanical response of brittle materials (see Appendix A for details). A
109 drawback of discretisations using randomly placed particles is that the simulated fractures
110 are jagged, whereas rock joints are often remarkably smooth. This aesthetic shortcoming
111 will in the future be resolved by the generation of progressively higher resolution models,

112 with smaller particle sizes. Discontinuum models with regular (e.g. cubic) particle packing
113 also permit the formation of straight fractures, but would however inhibit the formation
114 of non-planar fractures, which, as shown later, are an important feature in some of our
115 models.

116 **Figure 2**

117 In all our models the first fracture forms wherever the layer is weakest (discontinuum
118 models have heterogeneous strength distributions; see Appendix A) when the average
119 tensile stress within the layer reaches ~ 6.5 MPa (see Fig. A1), a tensile strength typical
120 for sedimentary rock (e.g. limestone, sandstone; Lockner, 1995). Failure within the matrix
121 is prevented so that matrix yielding and fracturing does not affect fracture within the
122 central layer. Layer-matrix interface geometries and frictional properties are represented
123 through a so-called 'smooth-joint' contact model (Itasca Consulting Group, Inc., 2008,
124 Mas Ivars et al., 2008) that implicitly replaces the irregular geometry of an interface
125 between domains within a particle assemblage with a planar discontinuity (Fig. 2). After
126 uniaxial confinement this three-layer model is extended horizontally with a velocity low
127 enough to assure quasi-static conditions, while maintaining a constant vertical stress of -5
128 MPa which, under lithostatic conditions and for an overburden density of 2500 kg/m^3 , is
129 equivalent to a depth of ~ 200 m (Fig. 2); our results are however applicable to a broader
130 range of confining pressure and tensile strength because the controlling factor is T/τ (see
131 below). Further details of the modelling are given in Appendix A.

132 We present results from four models with non-cohesive interfaces with friction coeffi-
133 cients μ of 0.2, 0.3, 0.5 and 0.8 and one model with a welded interface. All models attain
134 a finite strain of 0.008 and fracture saturation. The friction coefficients used in this study
135 cover the wide range reported by Byerlee (1978) for confining pressures of < 5 MPa, at
136 which the large variation in friction is due to variation in surface roughness. Although ex-
137 perimental constraints on the frictional properties of lithological interfaces (e.g. bedding
138 planes) are very sparse, we consider that the broad range, and in particular the lower
139 values, used in this study are appropriate. A range of interfacial shear strengths was

140 achieved by varying the interfacial friction coefficient, rather than the confining pressure,
 141 because the latter would also cause variations in both elastic properties and strength due
 142 to their pressure dependence (e.g. Schöpfer et al., 2009). The role of the interfacial friction
 143 in our models is simply to limit the interfacial shear stress; whether this is achieved in
 144 a natural system by interfacial slip and/or plasticity of the matrix layers depends on a
 145 wide range of extrinsic and intrinsic parameters. In fact, if the interfacial shear strength
 146 is greater than the shear strength of the matrix then the strength of the (plastic) matrix
 147 in shear is the controlling factor in determining fracture spacing (Kelly and Tyson, 1965).

148 2.2 Graphical representation

149 The model evolutions and their differences can be explored by generating the three types
 150 of plot presented in Fig. 3 for different models at different stages of their evolution.
 151 Animations of these plots of the five different models presented in this paper are provided
 152 as an electronic supplement. Each of these three forms of output are outlined below:

153 (i) Broken bonds and interface slip diagram: Shows the locations of sliding 'smooth-
 154 joint' contacts and broken bonds. If sliding occurs on a 'smooth-joint' contact, it is
 155 drawn as a horizontal line at the contact location, with a length equal to the area of
 156 the 'smooth-joint'. A sliding contact is defined as a contact where $|\mathbf{F}_s| > 0.99\mathbf{F}_n\mu$,
 157 where \mathbf{F}_n and \mathbf{F}_s are the contact normal (+ve) and shear force, respectively. Each
 158 broken bond, or 'crack', is drawn as a black line (Figs. 3 and 4) half-way between
 159 the two initially bonded particles, with a length equal to the average diameter of
 160 the two particles and perpendicular to a line joining the particle centres.

161 (ii) Horizontal normal stress plot: Shows the average horizontal normal stress (σ_x) dis-
 162 tribution within the central layer (as defined by Eq. C.1). The stress is normalised
 163 by the minimum layer tensile strength T_{min} , defined as the stress at which the first
 164 fracture forms (Fig. A1). If the layer strength and horizontal stress (σ_{xx}) distribu-
 165 tions were homogeneous, then subsequent fracturing would occur at the same stress
 166 level. However, the particulate nature of the model makes the material intrinsically

167 heterogeneous, so that the average horizontal normal stress can exceed T_{min} , i.e.
168 1.0 in the graph. Most importantly, if the heterogeneous σ_{xx} distribution controls
169 fracture, as in the high interfacial strength models, then fracture can occur at stress
170 levels which are significantly lower than the *average* layer strength.

171 (iii) Interfacial shear stress plot: Shows the interfacial shear stress distributions, ex-
172 pressed as the ratio of shear to normal stress, τ_{xy}/σ_{yy} , for each 'smooth-joint' con-
173 tact, with clockwise shear couples taken to be positive (Fig. 3). In case of the
174 cohesionless, frictional interface models the maximum value of this ratio is limited
175 by the friction coefficient, μ . We therefore plot $\tau_{xy}/\sigma_{yy}/\mu$ (i.e. $\tau_{xy}/(\mu\sigma_{yy})$), so that
176 the data plotted range from -1.0 to 1.0. Values of -1.0 or 1.0 hence indicate that
177 anti-clockwise and clockwise interfacial slip occurs, respectively.

178 **Figure 3**

179 **3 Results**

180 The fracture spacing and interfacial slip evolution of the discontinuum models with various
181 interfacial friction coefficients are shown in Figs. 4 and 5. The discontinuum model results
182 are compared with predictions based on a shear-lag model with interfacial slip which, in
183 the limit, yields a finite fracture spacing equivalent to the full-slip model (see Appendix
184 B and Appendix C).

185 **Figure 4 & 5**

186 *3.1 Low interfacial friction models ($\mu = 0.2$ and $\mu = 0.3$)*

187 For $\mu = 0.2$ and $\mu = 0.3$ (Fig. 5) there is good agreement between discontinuum and
188 shear-lag model predictions for the evolution of fracture spacing and reasonable agreement
189 for the proportion of slip (which is defined as the ratio of the sum of sliding 'smooth-joint'
190 contact areas to the sum of all 'smooth-joint' contact areas). This similarity of results

191 occurs because the dominant process in both models is mid-point fracture (Figs. 3 and
192 4).

193 The stress evolution in the low friction models is in close agreement with theoretical
194 considerations (Fig. 3; see also Appendix B). Once a fracture forms the average layer-
195 parallel normal stress at this location drops to zero and interfacial shear stresses develop
196 adjacent to the fracture. If the interfacial shear stress exceeds the shear strength interfacial
197 slip commences. In each fracture-bound block the shear sense is symmetric across a
198 horizontal mirror plane through the centre of the layer and a vertical mirror plane through
199 the centre of the block (Fig. 3a). The length of the slip regions decreases with increasing
200 interfacial shear strength (see first row in Fig. 4) and the vertical shear stress gradient
201 is balanced by a horizontal normal stress gradient, which is constant in the slip regions.
202 Fracture saturation in the low friction models occurs when slip occurs along the entire
203 interface as predicted by the *full-slip* model (compare Figs. 1b and 3b)

204 3.2 High interfacial friction models ($\mu = 0.5$ and $\mu = 0.8$)

205 For $\mu = 0.5$ and $\mu = 0.8$ (Fig. 5) there is poor agreement between discontinuum and
206 shear-lag model predictions (the deviation from the shear lag prediction is greater for the
207 higher friction model). The discontinuum modelling yields a much larger range of fracture
208 spacings during system evolution than the factor of 2 variation predicted by the shear lag
209 model and it produces a much lower average spacing at saturation.

210 **Figure 6**

211 Both of these discrepancies arise because 2-D heterogeneous stress distributions within
212 fracture-bound blocks, which are unaccounted for in the 1-D shear lag model, exert im-
213 portant controls on fracturing in the discontinuum models with high interface frictions.
214 Fracture saturation in the $\mu = 0.8$ discontinuum model arises largely by the same process
215 as described for the *2-D infill criterion* (compare Figs. 1c and 6b), i.e. infill fractures can
216 not propagate across a belt of compressive stress at the centre of a fracture block once a

217 critical s/t ratio is achieved (this critical s/t is $\ll 1.0$ in our models). However, the wider
218 range of fracture spacing than the factor of 2 variation prediction by mid-point fracture
219 throughout the evolution of the $\mu = 0.5$ and $\mu = 0.8$ discontinuum model is due to the
220 formation of new fractures close to existing fractures in blocks with $s/t \gg 1$ (Fig. 4).
221 Neither the shear lag nor CSC theories predict these new fractures, but their formation is
222 consistent with the commonly observed clustering of fractures in real layered materials. In
223 our models, the new fractures nucleate at interfaces and either propagate across the layer
224 to form through-going fractures or link with existing fractures to form splays/branches
225 (Fig. 6). They form when the maximum principal (least compressive) stress near the
226 interface is located in close proximity to the existing fractures (Groves et al., 1987, Hu
227 et al., 1993), rather than mid-way between them as predicted by 1-D analyses. The new
228 fractures propagate along curved principal stress trajectories that are convex towards the
229 earlier fracture (Fig. 6a). Such curved fractures are indeed observed in some laminates
230 (Groves et al., 1987, Hu et al., 1993).

231 *3.3 Reconciliation of fracture saturation theories*

232 Fracture spacings at saturation as predicted by the *1-D full-slip model* (Price's or Kelly-
233 Tyson equation), the *compressive stress criterion* (CSC) and the *2-D infill criterion*, and
234 as observed in discontinuum modelling, are compared in Fig. 7. There is good agreement
235 between the full-slip model and the discontinuum models at friction coefficients of $\mu < 0.4$
236 (Fig 7a). At higher friction coefficients, however, the discontinuum modelling predicts a
237 wider range of fracture spacing than the full-slip model and a lower average spacing.
238 Instead, the discontinuum model spacings here overlap with predictions of the alternative
239 2D infill criterion, which is thus shown to become more appropriate as welded interface
240 conditions are approached. Moreover, and in contrast to the unrealistic zero spacing
241 predicted by the full-slip model, the discontinuum model predicts spacings at saturation
242 in close agreement with the 2-D infill criterion at T/τ ratios approaching zero (i.e. a
243 welded interface; Fig 7b).

244 We presume that the T/τ value limiting the validity of 1-D approximations will be
245 greatly controlled by the size of existing flaws and may therefore vary widely as a function
246 of material heterogeneity (Tang et al., 2008).

247

Figure 7

248 4 Discussion

249 Distinct Element Method modelling of the fracturing of a brittle layer embedded in a
250 weaker matrix provides a rationale for the wide range of fracture characteristics observed
251 in nature (e.g. Sagy and Reches, 2006). With increasing layer parallel extension, new frac-
252 tures form in-between existing fractures, a process referred to as sequential infilling, until
253 no new fractures form when fracture saturation is reached. The resulting fracture dis-
254 tributions are often scale-dependent, with approximately regular fracture spacing which
255 scales with layer thickness, features which are typical of natural and man-made fracture
256 systems. Fracture spacing at saturation does, however, vary with the layer tensile to
257 interface shear strength ratio (T/τ) and is therefore not, as previous work has suggested,
258 an indicator of fracture system maturity or saturation (all models shown in the lowest
259 row in Fig. 4 are saturated). Conclusions about fracture saturation arising from numer-
260 ical models with predefined fractures that do not explicitly permit fracture nucleation,
261 propagation and associated interfacial slip (Bai and Pollard, 2000b) can, therefore, be
262 misleading. Variations in layer tensile to interface shear strength ratios (T/τ) can also
263 lead to changes in both fracture spacing populations and fracture geometries. At high T/τ
264 ratios fractures are straight, fracture spacings are quasi-periodic and fracture spacing to
265 layer thickness ratios at saturation range down to *ca.* 2 (Fig. 7), values which are typical
266 of many fracture systems. At lower T/τ , by contrast, fractures become more curved and
267 branched, clustered fracture patterns emerge and fracture spacing to layer thickness ra-
268 tios at saturation are often less than 1. Whilst existing analytical one-dimensional (1-D)
269 full-slip models are in good agreement with higher T/τ models, at lower T/τ interfacial
270 slip is suppressed and 2-D stress distributions within fracture-bound blocks controls fur-

271 ther fracture nucleation. Detailed analysis of the precise nature of fracture distributions
272 and shape, and how they change with mechanical parameters, such as T/τ ratio and layer
273 properties, is beyond the scope of this study but could have significant scientific and prac-
274 tical benefits. Our modelling shows, for example, that fracture branching and clustering
275 is not necessarily an indicator of either dynamic crack propagation (Sagy and Reches,
276 2006) or sub-critical crack growth (Olson, 2004). Branches and curved fractures in our
277 models nucleate at the layer interface and propagate towards existing straight fractures, a
278 scenario which was envisaged, but not investigated, in a study on fracture stepping across
279 interfaces (Cooke and Underwood, 2001). Perhaps the analysis of plume lines on natural
280 joint faces may reveal whether branched fracture geometries arise from either fracture
281 bifurcation or fracture linkage.

282 Our models reproduce many aspects of the geometry and evolution of fracture patterns
283 in single layers and also provide a basis for considering the potential impact of some other
284 factors:

285 (i) **Confining pressure and strength:** In this study we have explored the impact of
286 interfacial friction coefficient on fracturing in a three-layer system under a constant
287 confining pressure (Fig. 7a), defined by a constant layer-normal stress of -5 MPa
288 which is equivalent to ~ 200 m depth for lithostatic conditions and an overburden
289 density of 2500 kg/m^3 . In a horizontally layered sequence the interfacial shear
290 strength τ of cohesionless interfaces is the product of the vertical stress σ_v and the
291 friction coefficient μ , such that $|\tau| = \sigma_v \mu$. We expect, therefore, that similar relations
292 to those shown in Fig. 7 will arise for constant μ and for variable σ_v , which under
293 lithostatic conditions is given by γh (where γ is the specific weight of a rock column
294 extending down to a depth of h). If pore water is present then the *effective* vertical
295 stress is given by $\sigma'_v = \sigma_v(1 - \lambda_v)$, where λ_v is the ratio of pore fluid pressure p_f to
296 vertical stress σ_v (Sibson, 1998, Mandl, 2005). Under normal hydrostatic conditions
297 ($\lambda_v = 0.4$) an effective vertical stress of -5 MPa would hence be equivalent to a
298 depth of 340 m. The above relationships mean that for a constant interfacial friction

299 coefficient and layer tensile strength, a decrease in fracture spacing at saturation is
300 expected with increasing depth; the actual depth depends on overburden density and
301 pore pressure (Fig. 8). At certain depths, however, confining pressure inhibits the
302 formation of opening-mode fractures and there is a transition to shear fracturing
303 (Sibson, 1998, Ramsey and Chester, 2004, Schöpfer et al., 2007). By the same
304 token, in a sequence which is deformed at a constant confining pressure a systematic
305 decrease of fracture spacing will accompany a decrease in layer strength, until at a
306 certain strength a transition to shear failure will occur (Fig. 8).

307 (ii) **Interface cohesion:** The layer/matrix interfaces in our models are cohesionless,
308 a simplification which cannot always be justified in a natural system. We expect
309 that cohesion will decrease fracture spacing and that Price's full-slip model could
310 potentially overestimate saturation fracture spacing. Indeed, our ongoing discontinuum
311 modelling of cohesive interfaces suggests that the layer-parallel normal stress
312 profiles (Fig. 3ii) exhibit a central convex upwards region (corresponding to the
313 intact interface) which at the cusps exhibit a steeper slope than in the slip region
314 (Piggott, 1997). The tensile stress within this central region can be higher than for
315 a cohesionless interface and can hence cause further fracturing.

316 (iii) **Elastic properties and layer/matrix thicknesses:** Our modelling verifies Price's
317 *full-slip* model for cohesionless interfaces and high layer tensile to interface shear
318 strength ratios (T/τ). Because Price's model is solely based on a balance of me-
319 chanical forces under interfacial full-slip conditions, elastic properties and matrix
320 thicknesses have no impact on fracture spacing at saturation (the detailed evolution
321 of fracture spacing is theoretically dependent on these properties). The 2-D stress
322 distribution within fracture bound blocks under no-slip conditions is, however, sensi-
323 tive to the elastic properties (Bai and Pollard, 2000b) and layer/matrix thicknesses.
324 Consequently we expect slightly different results at low T/τ ratios for models with
325 different elastic properties and thickness ratios, though future work is required to

326 verify the nature of these dependencies.

327 (iv) **Multilayers:** Our models are for simple three-layer systems rather than the more
328 complex multilayered systems often found in nature. Geological studies suggest, for
329 example, that fracture pattern scaling may be hierarchical perhaps reflecting the
330 stacking patterns and mechanical amalgamation of fractured layers (e.g. Gillespie
331 et al., 2001). Experimental work on composite materials has shown that a fracture
332 in one layer can raise the stress in the adjacent layers and hence can lead to fracture
333 alignment, in particular when the matrix layers are thin (van den Heuvel et al.,
334 1997). The fracture-related interactions between different mechanical layers in a
335 layered sequence and their impact on fracture systematics could be the subject of
336 future studies using the same basic modelling approach described in this paper.

337 **Figure 8**

338 5 Conclusions

339 Our discontinuum models of fracture of single layers with various interfacial shear strength
340 suggests the following principal conclusions:

341 1. The validity and consequent applicability of Price's *full-slip* model, and similar
342 1-D approximations, depends on the ratio of layer tensile strength to interface shear
343 strength (T/τ).

344 (a) High T/τ ratios (*ca.* > 3.0 in our models) promote interfacial slip and yield
345 results that provide a good fit to a 1-D shear lag model.

346 (b) At lower strength ratios interfacial slip is suppressed and the heterogeneous
347 2-D stress distribution within fracture-bound blocks controls further fracture
348 nucleation (curved fractures, infill fractures).

349 2. In systems with high T/τ ratios the range of fracture spacing varies by a factor of two
350 because the dominant fracture mode is *mid-point fracturing*. Systems with lower

- 351 strength ratios exhibit a wider range of fracture spacing with a bimodal spacing
352 distribution due to the formation of curved fractures close to existing fractures.
- 353 3. The *compressive stress criterion* (CSC), or *stress transition theory*, appears not to
354 be valid since further infill fractures nucleate at the layer/matrix interfaces and
355 propagate through the centre of the fracture-bound blocks, hence the *2-D infill*
356 *criterion* is more appropriate.
- 357 4. Fracture saturation spacing decreases non-linearly with increasing interface shear
358 strength and therefore decreases with increasing effective layer normal stress, e.g.
359 overburden pressure.
- 360 5. In a layered sequence that permits interfacial slip, fracture spacing is not an indicator
361 of fracture system maturity, or saturation, i.e. a fracture spacing to layer thickness
362 ratio of $\gg 1$ does not imply that the system is unsaturated.

363 **Acknowledgements**

364 We thank C. Bean, M. Gilchrist, E. Holohan, T. Manzocchi and G. O'Brien (UCD), and T.
365 Engelder (Penn State) for fruitful discussions. The staff of Itasca, in particular P. Cundall,
366 D. Mas Ivars, M. Pierce and D. Potyondy, is acknowledged for valuable suggestions and
367 for providing additional PFC-2D licenses and software training. Thorough reviews by G.
368 Lloyd (Leeds) and D. Pollard (Stanford) are appreciated. This work was funded by Science
369 Foundation Ireland (SFI) research grants 07/RFP/GEOF340 and 08/RFP/GEO1170.

370 **Notation**

d	thickness of matrix layers
E_f	Young's modulus of fractured layer
e	model strain
e_m	matrix strain
e_p	pre-strain
g	average layer-parallel normal stress gradient
G_m	shear modulus of matrix
L	half-length of fracture-bound block
L_c	critical half-length of fracture-bound block
m	fraction of no-slip region
s	fracture spacing
t	thickness of fractured layer
T	tensile strength of fractured layer

371

α	fraction of area occupied by particles
β	load transfer parameter
μ	interfacial friction coefficient
σ_p	pre-stress
σ_x	average layer-parallel normal stress in fractured layer
σ_{xx}	layer-parallel normal stress component
σ_{xx}^p	layer-parallel normal stress component of particles
σ_y	interfacial normal stress
τ	interfacial shear strength
τ_x	interfacial shear stress

372 **Appendix A Distinct Element Method**

373 *A.1 Particle properties and boundary conditions*

374 The modelling in this study was performed with the PFC-2D software, which implements
375 the Distinct Element Method (DEM). The models were generated using the sample gen-
376 eration procedure detailed in Potyondy and Cundall (2004). The model boundaries are
377 rigid and frictionless. Particles have a uniform size distribution with a particle size range
378 of 0.0015-0.0025 m and comprise a model area fraction of 0.84. All particle contacts have
379 a contact friction coefficient of 0.5 and are assigned a linear contact model. Particle and
380 bond Young's moduli are equal and are 50.00 and 16.67 GPa within the central layer
381 and matrix, respectively. The particle and bond normal to shear stiffness ratio is 2.5 and
382 the modulus-stiffness scaling relations given in Potyondy and Cundall (2004) are applied.
383 Bonds between particles comprising the matrix have infinite bond strength and bonds
384 within the central layer have a tensile and shear strength of 20 MPa. Despite the con-
385 stant bond strength parameters, variations in local strength arise from changes in local
386 particle packing, with the resulting heterogeneity being an intrinsic feature of bonded
387 particle models. Accelerating motion is damped with a damping constant of 0.7. After a
388 bonded-particle model is generated with an initial isotropic stress of -0.1 MPa, contacts
389 between particles comprising the layer and matrix are assigned a 'smooth-joint' model,
390 which simulates the behaviour of a horizontal interface regardless of the local contact
391 plane orientations along the interface (Fig. 2). The area of each 'smooth-joint' contact
392 is scaled so that the sum of all contact areas is equal to the total length of the interface
393 represented as 'smooth-joints'. The model is then confined vertically, with zero interfacial
394 friction, until the desired confining pressure of -5 MPa is reached. If during confinement
395 or later extension a new contact between a matrix and layer particle is formed (e.g. due
396 to shear displacement) this contact is assigned a 'smooth-joint' model, otherwise spurious
397 contact forces would develop due to asperity lockup. After confinement particles touching
398 the lateral boundaries and their neighbours (black particles in Fig. 2) are assigned a hor-

399 izontal outward finite velocity of 0.005 m/s (this finite velocity is reached incrementally
400 in order to minimize dynamic effects) and the model specific 'smooth joint' friction and
401 cohesion are assigned. During extension the vertical confinement is maintained using a
402 servo-algorithm.

403 **Figure A1**

404 *A.2 Mechanical properties of central layer*

405 Average stresses and strains are measured in three circular regions within the central layer
406 using so-called measurement circles (Itasca Consulting Group, Inc., 2008, Potyondy and
407 Cundall, 2004, see inset in Fig. A1). These average stress data are used for determining
408 the macroscopic mechanical properties (modulus, strength) of the central layer. A plot
409 of average layer-parallel stress within these three measurement circles vs. model strain is
410 shown in Fig. A1. For each model, various parameters were determined using the average
411 of the three measurement circle data, and are summarised in Table A1. Initial uniaxial
412 confinement ($\sigma_y = -5$ MPa) leads to a horizontal pre-stress σ_p due to Poisson's effect
413 (Poisson's ratio under uniaxial loading and plane-stress conditions is $\nu = \sigma_p/\sigma_y$). Model
414 extension causes an increase in horizontal stress until the first fracture develops. The stress
415 level at which the first fracture develops is interpreted to be the minimum layer tensile
416 strength, T_{min} , under *homogeneous* stress conditions. The fact that the three curves in Fig.
417 A1 are basically identical until fracturing commences indicates that the stress distribution
418 is initially homogeneous. However, the stress-strain curves change their slopes when σ_x
419 becomes tensile, at a pre-strain e_p , and hence suggest that Young's modulus depends on
420 the sign of the least compressive stress. Young's modulus, under plane-stress conditions,
421 is the slope of the stress-strain curve, $\Delta\sigma_x/\Delta e_x$. When all stresses are compressive, the
422 secant Young's modulus is $E_p = -\sigma_p/e_p$, whereas when the least compressive stress is
423 tensile Young's modulus is $E_f = T_{min}/\Delta e$, where $\Delta e = e - e_p$. We use the latter modulus
424 for fitting the shear lag model.

425 **Table A1**

426 It is important to note that formulation of the shear lag model described in Appendix
427 B predicts zero stress for zero matrix strain. In the fitting procedure given in Appendix
428 C we therefore use $e_m = e - e_p$, i.e. the pre-strain is subtracted from the model strain.
429 In the plots shown in Fig. 5, this pre-strain is then added to the shear lag prediction.

430 **Appendix B Shear lag model**

431 *B.1 Geometry and boundary conditions*

432 Consider a periodically layered sequence of alternating 'soft' (so-called 'matrix') and
433 'strong' materials which are fractured (Fig. B1a). The matrix layers have a thickness
434 d and a shear modulus G_m . The fractured layers have a thickness t and a Young's mod-
435 ulus E_f . The fractures are equally-spaced with a spacing s , but because of the symmetry
436 of the problem we use the half-length L throughout this Appendix.

437 **Figure B1**

438 The boundary conditions acting on a 'unit-cell' are schematically illustrated in Fig.
439 B1a. A layer-parallel axial stress is induced in the system by displacing the ends of the
440 matrix layers, while keeping the fractures traction free. The average strain in the matrix
441 is e_m . This boundary condition leads to a layer-parallel tensile stress within the fracture-
442 bound block, with a maximum in the centre. An interfacial shear stress also develops, as
443 indicated with half-arrows in Fig. B1a, which decreases in a vertical direction and becomes
444 zero along horizontal lines centred in the matrix layers. Because the shear stresses acting
445 along one interface are opposite in sign on either side of the fracture-bound block (Fig.
446 B1a), the shear stress along a vertical line centred in the block must vanish.

447 To approximate this 2-D problem, stresses and strains are interpreted in an average,
448 rather than local sense, so that the shear lag model is a 1-D approximation. The *average*
449 horizontal, or layer-parallel, normal stress σ_x within a layer of thickness t centred at y_0 is
450 defined as (e.g. Iyer and Podladchikov, 2009)

$$\sigma_x(x) = \frac{1}{t} \int_{y_0-t/2}^{y_0+t/2} \sigma_{xx}(x, y) \, dy \quad (\text{B.1})$$

451 where σ_{xx} is the horizontal normal stress component. The shear stress within the
 452 fractured layer varies approximately linear with y (Fig. B1a). Mechanical equilibrium
 453 demands that a gradient in horizontal normal stress, $d\sigma_x/dx$, within the layer is balanced
 454 by an interfacial shear stress, τ_x .

$$\frac{d\sigma_x}{dx} + \frac{\tau_x^{top} - \tau_x^{bot}}{t} = 0 \quad (\text{B.2})$$

455 The superscripts refer to the shear stress acting on the top and bottom layer interface.
 456 If the top and bottom interfacial shear stresses are identical in magnitude, but opposite
 457 in sign, then Eq. B.2 can be written as

$$\frac{d\sigma_x}{dx} = -\frac{2\tau_x}{t} \quad (\text{B.3})$$

458 A positive normal stress gradient hence leads to a negative (counter-clockwise) shear
 459 stress along the *upper* interface (Fig. B1a).

460 We assume that the maximum interfacial shear stress, τ , is given by a Coulomb limit

$$|\tau| = \sigma_y \mu, \quad (\text{B.4})$$

461 where σ_y is the normal stress acting on the interface and μ is the interfacial friction
 462 coefficient.

463 *B.2 No-slip solution*

464 Cox (1952) derived a solution that conforms with the boundary conditions outlined above.
 465 In the absence of interfacial slip the average layer-parallel normal stress within a fracture-
 466 bound block is

$$\sigma_x(x) = E_f e_m \left(1 - \frac{\cosh(\beta(L-x))}{\cosh(\beta L)} \right) \quad (\text{B.5})$$

467 where β is the load transfer parameter. For the sake of mathematical brevity the
 468 origin ($x = 0$) in Eq. B.5 is located at the left hand fracture. If the shear stress in the
 469 matrix decreases linearly in a vertical direction from its maximum value at the interface
 470 to zero midway between two fracturing layers (Fig. B1a) then β is (Ji et al., 1998)

$$\beta = \sqrt{\frac{8G_m}{E_f t d}} \quad (\text{B.6})$$

471 where G_m is the shear modulus of the matrix. The actual shear stress may decrease
 472 non-linearly and various analytical solutions have been postulated to take a non-linear
 473 shear stress decay into account (Ji and Saruwatari, 1998, Jain et al., 2007). We prefer,
 474 however, to determine the value of β in our models directly as outlined in Appendix C.

475 The maximum layer-parallel normal stress within the fractured block, σ_{max} , occurs in
 476 the centre ($x = L$) and given by

$$\sigma_{max} = E_f e_m (1 - \text{sech}(\beta L)) \quad (\text{B.7})$$

477 The shear stress acting on the interface, τ_x , can be obtained by differentiating Eq. B.5
 478 and substituting the result into Eq. B.3.

$$\tau_x(x) = \frac{t}{2} E_f e_m \beta \frac{\sinh(\beta(L-x))}{\cosh(\beta L)} \quad (\text{B.8})$$

479 where the absence of the minus sign indicates that Eq. B.8 describes the shear stress
 480 distribution along the *lower* interface. The maximum interface shear stress, τ_{max} , occurs
 481 at the end of the fractured block ($x = 0$) and is

$$\tau_{max} = \frac{t}{2} E_f e_m \beta \frac{\sinh(\beta L)}{\cosh(\beta L)} \quad (\text{B.9})$$

482 Average normal stress and interfacial shear stress profiles that were calculated using

483 these solutions are plotted in Fig. B1bi.

484 If we assume that the average normal stress in the fracturing layer cannot exceed the
 485 tensile strength, T , then a limiting, or *critical half-length* L_c , below which no fracturing
 486 can occur at a particular matrix strain, exists (Lloyd et al., 1982). The critical half-length,
 487 L_c , can then be obtained by replacing σ_{max} in Eq. B.7 with T and solving for L

$$L_c^{noslip} = \frac{1}{\beta} \operatorname{asech} \left(1 - \frac{T}{E_f e_m} \right) \quad (\text{B.10})$$

488 where the superscript *noslip* denotes that this is the critical half-length for a welded
 489 interface. For infinite matrix strain Eq. B.10 becomes

$$\lim_{e_m \rightarrow \infty} L_c^{noslip} = 0$$

490 which is clearly not possible, but sometimes used as an argument against the shear
 491 lag model (Bai et al., 2000). However, interfacial slip will occur if the maximum interface
 492 shear stress, τ_{max} , exceeds the shear strength of the interface, τ (Ji et al., 1998, Jain
 493 et al., 2007). The matrix strain at which interfacial slip commences can be obtained by
 494 substituting the critical half-length for a welded interface (Eq. B.10) as L into Eq. B.9
 495 and replacing τ_{max} with τ . Solving for e_m and simplifying gives

$$e_m^{sliponset} = \frac{4\tau^2 + (T\beta t)^2}{2E_f T(\beta t)^2} \quad (\text{B.11})$$

496 From this point onwards the interface is comprised of two regions, (I) slip, or plastic,
 497 regions near the fractures and (II) a no-slip, or elastic, region in the centre of the fractured
 498 block (Fig. B1bii). In the limit, the entire interface will be sliding (Fig. B1biii).

499 The critical half-length at the onset of slip can be obtained by substituting the matrix
 500 strain at the onset of slip given by Eq. B.11 into Eq. B.10 and is

$$L_c^{sliponset} = \frac{1}{\beta} \operatorname{asech} \left(\frac{4\tau^2 - (T\beta t)^2}{4\tau^2 + (T\beta t)^2} \right) \quad (\text{B.12})$$

501 Eq. B.12 indicates that the interfacial shear strength τ must have a certain minimum
 502 value (the numerator in the inverse hyperbolic secant term must be > 0), otherwise the
 503 entire interface will slip as soon as the first fracture appears and no further fracture is
 504 possible.

$$\tau > \frac{T\beta t}{2} \quad (\text{B.13})$$

505 This inequality can alternatively be obtained by the condition that the matrix strain
 506 at the onset of fracture must be less than the strain at the onset of interfacial slip (Eq.
 507 B.11), i.e. $e_m^{sliponset} > T/E_f$.

508 *B.3 Full-slip solution*

509 If the normal stress acting on the interface, σ_y , remains constant and uniform while slip
 510 occurs, then the shear stress acting on the interface is also constant and given by Eq. B.4.
 511 As a consequence the gradient of the layer-parallel normal stress within the fracture layer
 512 is constant, i.e. the layer-parallel stress profile is a triangle (Eq. B.3; see Fig. B1biii).
 513 The normal stress is, however, limited by the tensile strength, T , so that $d\sigma_x/dx$ in Eq.
 514 B.3 can be replaced by T/L . The critical half-length of the fractured block, below which
 515 no further fracture can occur, is therefore given by

$$L_c^{fullslip} = \frac{Tt}{2\tau} \quad (\text{B.14})$$

516 Eq. B.14 is known as Price's model in Earth Sciences (Price, 1966, Mandl, 2005) and
 517 as Kelly-Tyson equation in Material Sciences (Kelly and Tyson, 1965, Tripathi and Jones,
 518 1998).

519 *B.4 Partial-slip solution*

520 It is clear that the two models outlined above, i.e. the no-slip and the full-slip solution,
 521 are end-member scenarios. The onset of interfacial slip is derived above and given by Eq.

522 B.11. An increase in extension leads to a progressive increase of the length of the slip
 523 region until, in theory, the entire interface is sliding.

524 Here we use a Piggott model (Piggott, 1978, Huang and Young, 1995, van den Heuvel
 525 et al., 1997) where a linear stress build-up (Eq. B.3) in the slip region is immediately
 526 followed by an elastic stress build-up according to Cox's shear lag model (Eq. B.5).

$$\sigma_x(x) = \begin{cases} \frac{2\tau}{t}x = gx & 0 \leq x \leq x_t \\ gx_t + (E_f e_m - gx_t) \left(1 - \frac{\cosh(\beta(L-x))}{\cosh(\beta(L-x_t))}\right) & x_t \leq x \leq L \end{cases} \quad (\text{B.15})$$

527 where x_t is the transition point from the slip to no-slip region and g is the normal
 528 stress gradient in the slip region, which is a constant, and used here for brevity. Eq. B.15
 529 is, again, given for the left-hand side of a fracture-bound block with the left-hand fracture
 530 located at $x = 0$. Notice that Eq. B.15 becomes Cox's solution (Eq. B.5) if $x_t = 0$ and
 531 that the full-slip solution (Eq. B.14) is obtained when $e_m = \infty$.

532 The maximum layer-parallel normal stress occurs at the centre of the bonded region,
 533 at L , and is given by

$$\sigma_{max} = gx_t + (E_f e_m - gx_t)(1 - \text{sech}(\beta(L-x_t))) \quad (\text{B.16})$$

534 Analogous to the no-slip case, the shear stress acting on the interface, τ_x , can be
 535 obtained by differentiating Eq. B.15 and substituting the result into Eq. B.3.

$$\tau_x(x) = \begin{cases} \tau & 0 \leq x \leq x_t \\ \frac{t}{2}(E_f e_m - gx_t)\beta \frac{\sinh(\beta(L-x))}{\cosh(\beta(L-x_t))} & x_t \leq x \leq L \end{cases} \quad (\text{B.17})$$

536 The maximum interfacial shear stress, τ_{max} , occurs at the end of the bonded region
 537 ($x = x_t$) and is given by

$$\tau_{max} = \frac{t}{2}(E_f e_m - g x_t) \beta \frac{\sinh(\beta(L - x_t))}{\cosh(\beta(L - x_t))} \quad (\text{B.18})$$

538 The critical half-length is determined by limiting the maximum normal stress given
 539 by Eq. B.16 by the tensile strength T and solving for L .

$$L_c^{partialslip} = x_t + \frac{1}{\beta} \operatorname{asech} \left(\frac{T - E_f e_m}{g x_t - E_f e_m} \right) \quad (\text{B.19})$$

540 For a *cohesionless* interface (Eq. B.4) the unknown x_t can be evaluated by assuming
 541 stress continuity at the transition point, for which the maximum interface shear stress (Eq.
 542 B.18) is equal to the shear strength τ . For a cohesive interface stress continuity cannot
 543 be justified and an interfacial shear stress jump and an associated increase of the average
 544 layer-parallel normal stress gradient occurs (Huang and Young, 1995, van den Heuvel
 545 et al., 1997). In the present study, however, the effect of cohesion is not investigated and
 546 we therefore assume that the interfacial shear strength is provided by friction only.

547 Taking τ as τ_{max} in Eq. B.18 and substituting L , as given by Eq. B.19, gives after
 548 rearrangement.

$$2\tau - \beta t \sqrt{(g x_t - T)(g x_t + T - 2E_f e_m)} = 0 \quad (\text{B.20})$$

549 Unfortunately a closed form solution for Eq. B.20 does not exist and therefore x_t has
 550 to be determined numerically. The result can then be substituted into Eq. B.19 and the
 551 critical half-length for the partial-slip case can be obtained. Average normal stress and
 552 interfacial shear stress profiles that were calculated using these solutions are plotted in
 553 Fig. B1bii.

554 B.5 Implementation

555 The critical half-length, L_c and, if slip occurs, the length of the slip region, x_t , can be
 556 calculated as a function of matrix strain using a simple computer program (a MATLAB
 557 script can be obtained upon request from the corresponding author). The input parame-

558 ters are the layer thicknesses, t and d , the elastic properties, E_f and G_m , the layer tensile
 559 and interface shear strengths, T and τ , respectively, and the matrix strain, e_m . The
 560 algorithm is structured as follows:

If $E_f e_m > T$ And $\tau > T\beta t/2$ (Eq. B.13) Then

If $e_m \leq e_m^{slip\ onset}$ (Eq. B.11) Then

Calculate L_c^{noslip} (Eq. B.10), $x_t = 0$

Else

Determine x_t numerically (Eq. B.20) and calculate $L_c^{partialslip}$ (Eq. B.19)

EndIf

EndIf

561 The first if-statement checks (i) whether the strain is high enough to exceed the tensile
 562 strength of the layer and (ii) whether the interfacial shear strength is high enough. The
 563 second if-statement checks whether the strain is less than the onset of interfacial slip or
 564 not. If no-slip occurs, then the no-slip solution is used, otherwise the partial-slip solution
 565 is used for calculating L_c and x_t .

566 A plot of L_c and x_t vs. e_m is shown in Fig. B1c. As expected, the critical-half-length
 567 decreases with increasing strain and asymptotically approaches the full-slip solution. The
 568 length of the slip region gradually increases and eventually becomes equal to the full-slip
 569 half-length. If interfacial slip were inhibited, then L_c asymptotically approaches 0.

570 Appendix C Fitting shear lag model to numerical modelling results

571 An approximation of the average stress, as given by Eq. B.1, within the particle model is
 572 obtained by interpolating the horizontal particle stress components, σ_{xx}^p , on a square-grid
 573 with a spacing $\Delta x = \Delta y = 0.0025$ and applying Simpson's rule

$$\sigma_x(x) \cong \alpha \frac{1}{t} \sum_{n=0}^N \sigma_{xx}^p \left(y_0 - \frac{t}{2} + \frac{\Delta y}{2} + \Delta y n \right), \quad \text{where } N = \frac{t}{\Delta y} - 1 \quad (\text{C.1})$$

574 where α is the fraction of area occupied by particles ($\alpha = 0.84$ in our models).

575 For each fracture-bound block a shear lag model with partial slip (Section B.4) is
576 fitted to the approximate average stress data to obtain an estimate for the load transfer
577 parameter β (Fig. 3). First the magnitude and location of the maximum horizontal normal
578 stress σ_{max} is calculated by fitting a 2^{nd} -order polynomial to six consecutive points. The
579 stress profiles are often asymmetric, hence the best-fit β -value is calculated for the right
580 and left hand side separately. Each side has a length of L , which is comprised of a
581 slip-region with length x_t and a no-slip region with length mL , where $m = 1 - x_t/L$.

582 Again, we assume stress continuity from the slip to no-slip region, so that the maximum
583 shear stress at the ends of the no-slip region τ_{max} is equal to the interface shear strength
584 τ . Using $2\tau/t$ instead of g and mL instead of $(L - x_t)$ in Eq. B.18 and solving for x_t gives

$$x_t = \frac{E_f e_m t}{2\tau} - \frac{\cosh(mL\beta)}{\beta \sinh(mL\beta)} \quad (\text{C.2})$$

585 Substitution of Eq. C.2 into Eq. B.16 and using again mL instead of $(L - x_t)$ gives

$$E_f e_m - \frac{2\tau}{t\beta} \cosh(mL\beta) \frac{\text{sech}(mL\beta)}{\sinh(mL\beta)} - \sigma_{max} = 0 \quad (\text{C.3})$$

586 The β -value can be determined numerically from Eq. C.3 and x_t can then be calculated
587 using Eq. C.2. The best-fit β -value is obtained by iteratively varying m in the range of
588 0.0 to 1.0 and minimising the sum-of-squares σ_x differences between model profile and
589 shear lag equation (Eq. B.15).

590 It is important to note that the condition $\tau_{max} = \tau$ can only be justified if interfacial
591 slip actually occurs (prior to interfacial slip $\tau_{max} < \tau$). In addition β is poorly constrained
592 when slip occurs over almost the entire length of a fracture-bound block (e.g. at fracture
593 saturation). Hence the best-fit β -value used for predicting the fracture and slip evolution
594 (Fig. 5) is the arithmetic mean of all best-fit β -values where $0.1 < x_t/L < 0.9$. The
595 best-fit β -values for all four models are provided in Fig 5a.

References

- Adda-Bedia, M., Amar, M. B., 2001. Fracture spacing in layered materials. *Physical Review Letters* 86, 5703–5706.
- Altus, E., Ishai, O., 1986. Transverse cracking and delamination interaction in the failure process of composite laminates. *Composites Science and Technology* 26, 59–77.
- Bai, T., Pollard, D. D., 2000a. Closely spaced fractures in layered rocks: initiation mechanism and propagation kinematics. *Journal of Structural Geology* 22, 1409–1425.
- Bai, T., Pollard, D. D., 2000b. Fracture spacing in layered rocks: a new explanation based on the stress transition. *Journal of Structural Geology* 22, 43–57.
- Bai, T., Pollard, D. D., Gao, H., 2000. Explanation for fracture spacing in layered materials. *Nature* 403, 753–756.
- Berthelot, J.-M., 2003. Transverse cracking and delamination in cross-ply glass-fiber and carbon-fiber reinforced plastic laminates: Static and fatigue loading. *Applied Mechanics Reviews* 56, 111–147.
- Berthelot, J.-M., Leblond, P., El Mahi, A., Le Corre, J. F., 1996. Transverse cracking of cross-ply laminates: Part 1. Analysis. *Composites Part A: Applied Science and Manufacturing* 27, 989–1001.
- Bourne, S. J., 2003. Contrast of elastic properties between rock layers as a mechanism for the initiation and orientation of tensile failure under uniform remote compression. *Journal of Geophysical Research* 108, (B8)2395.
- Byerlee, J., 1978. Friction of rocks. *Pure and Applied Geophysics* 116, 615–626.
- Cooke, M. L., Underwood, C. A., 2001. Fracture termination and step-over at bedding interfaces due to frictional slip and interface opening. *Journal of Structural Geology* 23, 223–238.
- Cox, H. L., 1952. The elasticity and strength of paper and other fibrous materials. *British Journal of Applied Physics* 3, 72–79.
- Dharani, L. R., Wei, J., Ji, F. S., Zhao, J. H., 2003. Saturation of transverse cracking with delamination in polymer cross-ply composite laminates. *International Journal of Damage Mechanics* 12, 89–113.
- Garrett, K. W., Bailey, J. E., 1977. Multiple transverse fracture in 90° cross-ply laminates of a glass fibre-reinforced polyester. *Journal of Materials Science* 12, 157–168.
- Gillespie, P. A., Walsh, J. J., Watterson, J., Bonson, C. G., Manzocchi, T., 2001. Scaling relationships of joint and vein arrays from The Burren, Co. Clare, Ireland. *Journal of Structural Geology* 23, 183–201.
- Groves, S. E., Harris, C. E., Highsmith, A. L., Allen, D. H., Norvell, R. G., 1987. An experimental and analytical treatment of matrix cracking in cross-ply laminates. *Experimental Mechanics* 27, 73–79.
- Hobbs, D. W., 1967. The formation of tension joints in sedimentary rocks: an explanation. *Geological Magazine* 104, 550–556.
- Hu, S., Bark, J. S., Nairn, J. A., 1993. On the phenomenon of curved microcracks in [(S)/90_n]_s laminates: their shapes, initiation angles and locations. *Composites Science and Technology* 47, 321–329.
- Huang, Q., Angelier, J., 1989. Fracture spacing and its relation to bed thickness. *Geological Magazine* 126, 355–362.
- Huang, Y., Young, R. J., 1995. Interfacial behaviour in high temperature cured carbon fibre/epoxy resin model composite. *Composites* 26, 541–550.

- Itasca Consulting Group, Inc., 2008. PFC2D (Particle Flow Code in 2 Dimensions), Version 4.0. Minneapolis, MN.
- Iyer, K., Podladchikov, Y. Y., 2009. Transformation-induced jointing as a gauge for interfacial slip and rock strength. *Earth and Planetary Science Letters* 280, 159–166.
- Jain, A., Guzina, B. B., Voller, V. R., 2007. Effects of overburden on joint spacing in layered rocks. *Journal of Structural Geology* 29, 288–297.
- Ji, S., Saruwatari, K., 1998. A revised model for the relationship between joint spacing and layer thickness. *Journal of Structural Geology* 20, 1495–1508.
- Ji, S., Zhu, Z., Wang, Z., 1998. Relationship between joint spacing and bed thickness in sedimentary rocks: effects of interbed slip. *Geological Magazine* 135, 637–655.
- Kelly, A., Tyson, W. R., 1965. Tensile properties of fiber-reinforced metals: copper/tungsten and copper/molibdenum. *Journal of the Mechanics and Physics of Solids* 13, 329–350.
- Korach, C. S., Keer, L. M., 2002. Stresses between 3D fractures in infinite and layered elastic solids. *Engineering Fracture Mechanics* 69, 1815–1825.
- Ladeira, F. L., Price, N. J., 1981. Relationship between fracture spacing and bed thickness. *Journal of Structural Geology* 3, 179–183.
- Li, Y., Yang, C., 2007. On fracture saturation in layered rocks. *International Journal of Rock Mechanics and Mining Sciences* 44, 936–941.
- Lloyd, G. E., Ferguson, C. C., Reading, K., 1982. A stress-transfer model for the development of extension fracture boudinage. *Journal of Structural Geology* 4, 355–372.
- Lockner, D. A., 1995. Rock failure. In: Ahrens, T. J. (Ed.), *Rock Physics & Phase Relations. A Handbook of Physical Constants*. AGU Reference Shelf 3. American Geophysical Union, Washington DC, pp. 127–147.
- Mandal, N., Deba, S. K., Khan, D., 1994. Evidence for a non-linear relationship between fracture spacing and layer thickness. *Journal of Structural Geology* 16, 1275–1281.
- Manders, P. T., Chou, T.-S., Jones, F. R., Rock, J. W., 1983. Statistical analysis of multiple fracture in 00°/90°/0° glass fibre/epoxy resin laminates. *Journal of Materials Science* 18, 2876–2889.
- Mandl, G., 2005. *Rock Joints: The Mechanical Genesis*. Springer-Verlag, Heidelberg.
- Mas Ivars, D., Potyondy, D. O., Pierce, M., Cundall, P. A., 2008. The smooth-joint contact model. In: Schrefler, B., Perego, U. (Eds.), *Proceedings of WCCM8 - ECCOMAS 2008, (8th World Congress on Computational Mechanics/5th European Congress on Computational Methods in Applied Sciences and Engineering)*.
- Nairn, J. A., 2000. Matrix microcracking in composites. In: Talreja, R., Manson, J.-A. E. (Eds.), *Comprehensive Composite Materials Vol. 2: Polymer Matrix Composites*. Elsevier Science, Amsterdam, pp. 403–432.
- Narr, W., Suppe, J., 1991. Joint spacing in sedimentary rocks. *Journal of Structural Geology* 13, 1037–1048.
- Ohsawa, T., Nakyama, N., Miwa, M., Hasegawa, A., 1978. Temperature dependence of critical fiber length for glass fiber-reinforced thermosetting resins. *Journal of Applied Polymer Science* 22, 3203–3212.

- Olson, J. E., 2004. Predicting fracture swarms - the influence of subcritical crack growth and the crack-tip process zone on joint spacing in rock. In: Cosgrove, J. W., Engelder, T. (Eds.), *The Initiation, Propagation, and Arrest of Joints and Other Fractures*, Geol. Soc. Lond. Spec. Publ. 231. Geological Society, London, pp. 73–88.
- Parvizi, A., Bailey, J. E., 1978. On multiple transverse cracking in glass fibre epoxy cross-ply laminates. *Journal of Materials Science* 13, 2131–2136.
- Piggott, M. R., 1978. Expressions governing stress-strain curves in short fibre reinforced polymers. *Journal of Materials Science* 13, 1709–1716.
- Piggott, M. R., 1997. Why interface testing by single-fibre methods can be misleading. *Composites Science and Technology* 57, 965–974.
- Potyondy, D. O., Cundall, P. A., 2004. A bonded-particle model for rock. *International Journal of Rock Mechanics and Mining Sciences* 41, 1329–1364.
- Price, N. J., 1966. *Fault and Joint Development in Brittle and Semi-Brittle Rock*. Pergamon Press Ltd., Oxford.
- Ramsey, J. M., Chester, F. M., 2004. Hybrid fracture and the transition from extension fracture to shear fracture. *Nature* 428, 63–66.
- Sagy, A., Reches, Z., 2006. Joint intensity in layered rocks: The unsaturated, saturated, supersaturated and clustered classes. *Israel Journal of Earth Sciences* 55, 33–42.
- Savalli, L., Engelder, T., 2005. Mechanisms controlling rupture shape during subcritical growth of joints in layered rocks. *Geological Society of America Bulletin* 117, 436–449.
- Schoeppner, G. A., Pagano, N. J., 1999. 3-D thermoelastic moduli and saturation crack density for cross-ply laminates with transverse cracks. *International Journal of Damage Mechanics* 8, 273–309.
- Schöpfer, M. P. J., Abe, S., Childs, C., Walsh, J. J., 2009. The impact of porosity and crack density on the elasticity, strength and friction of cohesive granular materials: Insights from DEM modelling. *International Journal of Rock Mechanics and Mining Sciences* 46, 250–261.
- Schöpfer, M. P. J., Childs, C., Walsh, J. J., 2007. Two-dimensional distinct element modeling of the structure and growth of normal faults in multilayer sequences: 2. Impact of confining pressure and strength contrast on fault zone geometry and growth. *Journal of Geophysical Research* 112, B10404.
- Sibson, R. H., 1998. Brittle failure mode plots for compressional and extensional tectonic regimes. *Journal of Structural Geology* 20, 655–660.
- Tang, C. A., Liang, Z. Z., Zhang, Y. B., Chang, X., Tao, X., Wang, D. G., Zhang, J. X., Liu, J. S., Zhu, W. C., Elsworth, D., 2008. Fracture spacing in layered materials: a new explanation based on two-dimensional failure process modeling. *American Journal of Science* 308, 49–72.
- Tripathi, D., Jones, F. R., 1998. Single fibre fragmentation test for assessing adhesion in fibre reinforced composites. *Journal of Materials Science* 33, 1–16.
- van den Heuvel, P. W. J., Peijs, T., Young, R. J., 1997. Failure phenomena in two-dimensional multifibre microcomposites: 2. A raman spectroscopic study of the influence of inter-fibre spacing on stress concentrations. *Composites Science and Technology* 57, 899–911.
- Wu, H., Pollard, D. D., 1995. An experimental study of the relationship between joint spacing and layer thickness. *Journal of Structural Geology* 17, 887–905.

Tables

μ	e_p	σ_p (MPa)	E_p (GPa)	E_f (GPa)	T (MPa)
0.2	0.0000290	-1.65	56.95	36.18	6.68
0.3	0.0000298	-1.66	55.79	35.35	6.38
0.5	0.0000293	-1.68	57.30	36.47	6.25
0.8	0.0000295	-1.66	56.11	35.42	6.62
Mean	0.0000294	-1.66	56.54	35.85	6.48

Table A1: Material and model parameters obtained from measurement circles (see Fig. A1) for four models with different interfacial friction coefficients, μ .

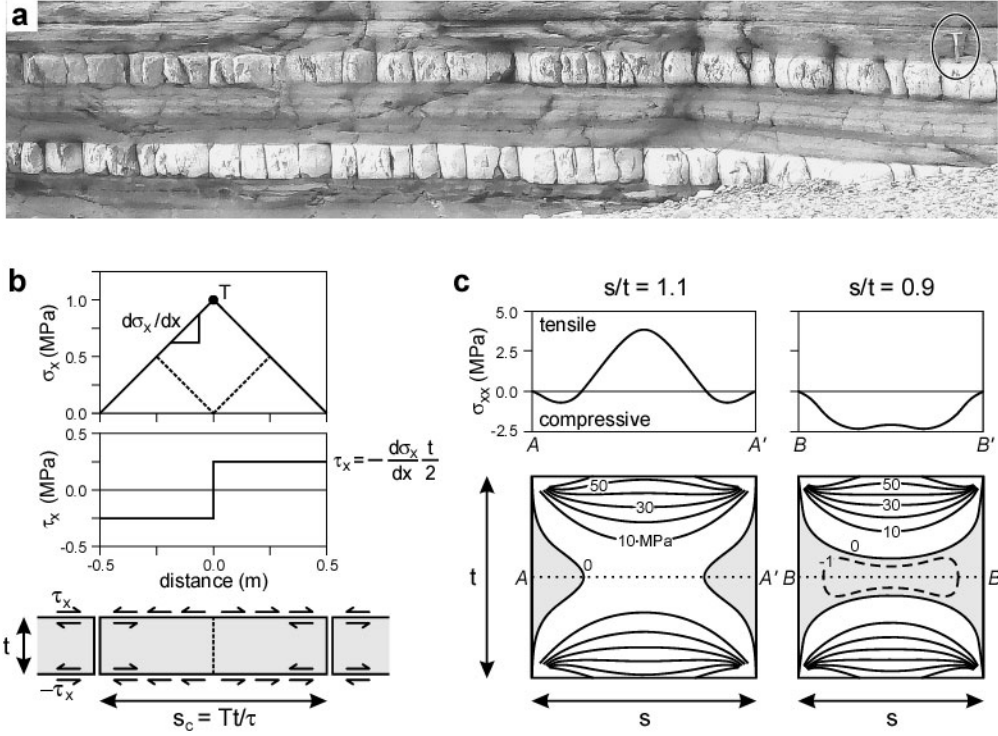


Figure 1: Natural example of layer-confined opening fractures and illustrations of theories for fracture saturation. **a**, Field example of rock joints (opening fractures) developed within limestone beds (pale) embedded in mudrocks (grey) exposed in Lillstock Bay, Somerset, UK. Rock hammer (circled) is 0.29 m long. **b**, *Full-slip*, or frictional coupling, model (Kelly and Tyson, 1965, Price, 1966). A constant interfacial shear stress τ_x is balanced by a layer-parallel normal stress gradient $d\sigma_x/dx$. The normal stress is limited by the layer tensile strength T which leads to a critical fracture spacing s_c below which no further fracture can occur. The dashed lines indicate that the minimum fracture spacing is $0.5s_c$. **c**, *Compressive stress criterion* (Dharani et al., 2003), or *stress-transition theory* (Bai et al., 2000, Bai and Pollard, 2000b). If no interfacial slip occurs, a region of compressive layer-parallel normal stress σ_{xx} (grey areas) that extends across the central area of the fracture-bound block develops at a fracture spacing to thickness ratio (s/t) of ~ 1.0 (modified after Bai and Pollard, 2000a,b)

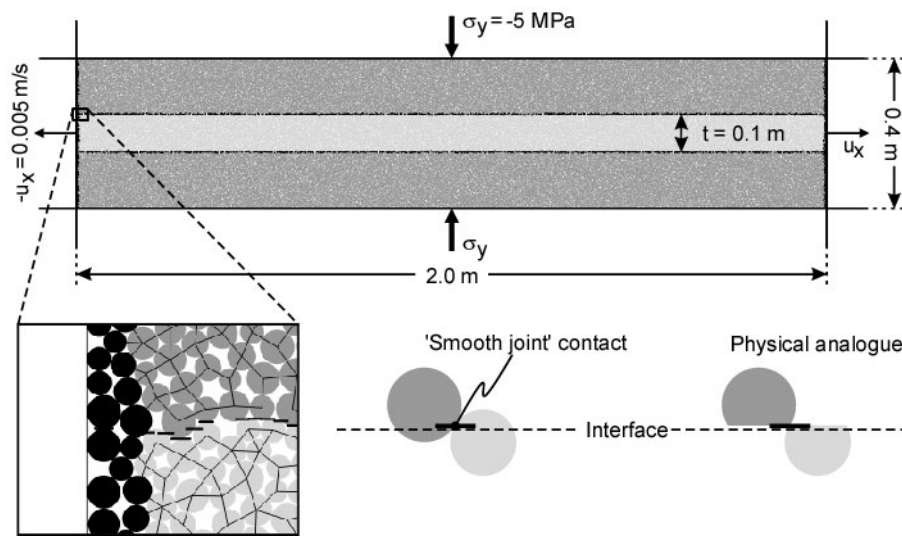


Figure 2: Numerical model and its boundary conditions used for modelling rock joints. Dark and light grey particles comprise the matrix and central layer, respectively, and black particles are lateral boundaries to which a horizontal velocity is applied. Black lines joining particle centres are bonds and bold horizontal lines at the layer interface are 'smooth-joint' contacts (see inset). σ_y , vertical applied boundary stress. u_x , horizontal applied boundary velocity. t , thickness of central layer.

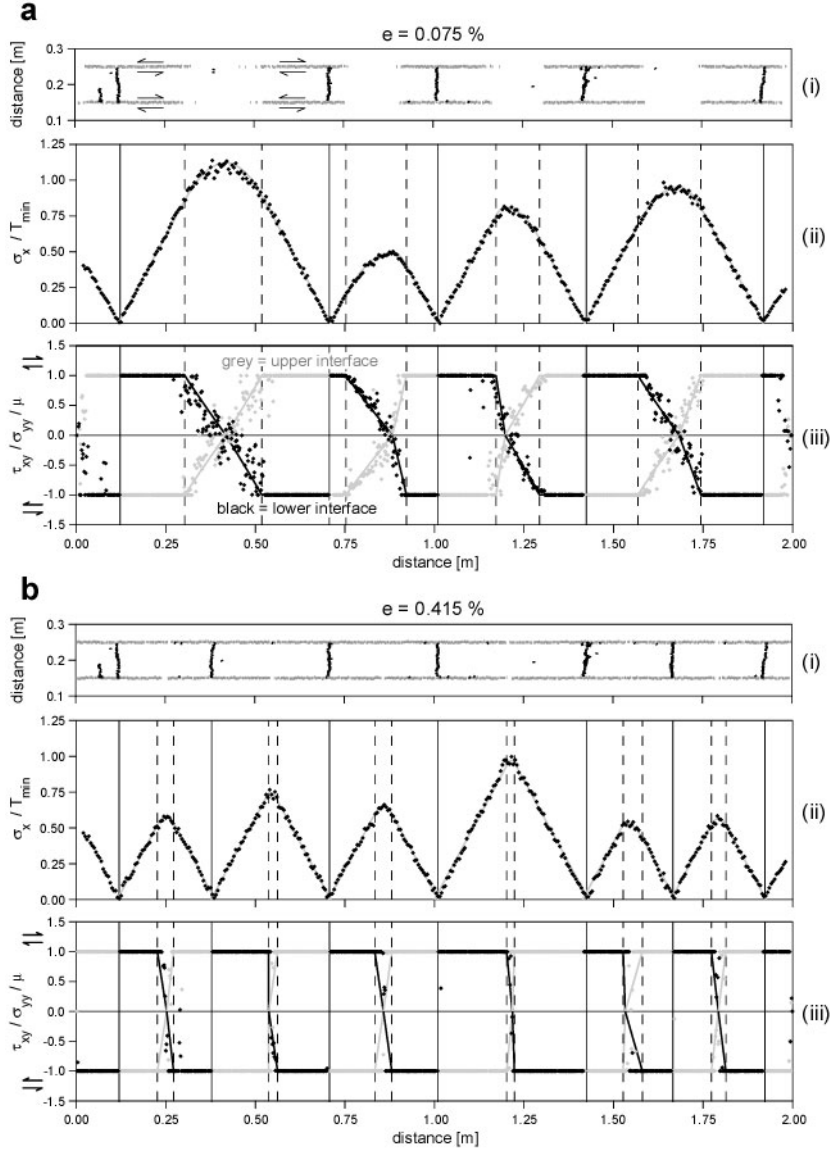


Figure 3: Average layer-parallel normal stress and interfacial shear stress distribution in discontinuum model with low interface friction coefficient ($\mu = 0.3$) at (**a**) $e = 0.075\%$ and (**b**) $e = 0.415\%$. (i) Locations of broken bonds (black) and sliding 'smooth-joint' contacts (grey). The sense of shear is indicated with half arrows for one fracture-bound block. (ii) Average horizontal, or layer-parallel, stress in fracture layer (σ_x) normalised by the minimum tensile strength (T_{min}). Black dots are model stress data and grey lines are best-fit shear lag model profiles. (iii) Interface shear stress to normal stress ratio (τ_{xy}/σ_{yy}) normalised by interface friction coefficient (μ). Black and grey dots are 'smooth-joint' contact stress data of the lower and upper interface, respectively. Solid lines are best-fit shear lag model solutions. Positions of fractures and slip to no-slip regions are indicated with vertical solid and dashed lines, respectively. See Appendix C for details regarding the best-fit shear lag model. Animations of graphical representation for this and a selection of other models are provided as an electronic supplement.

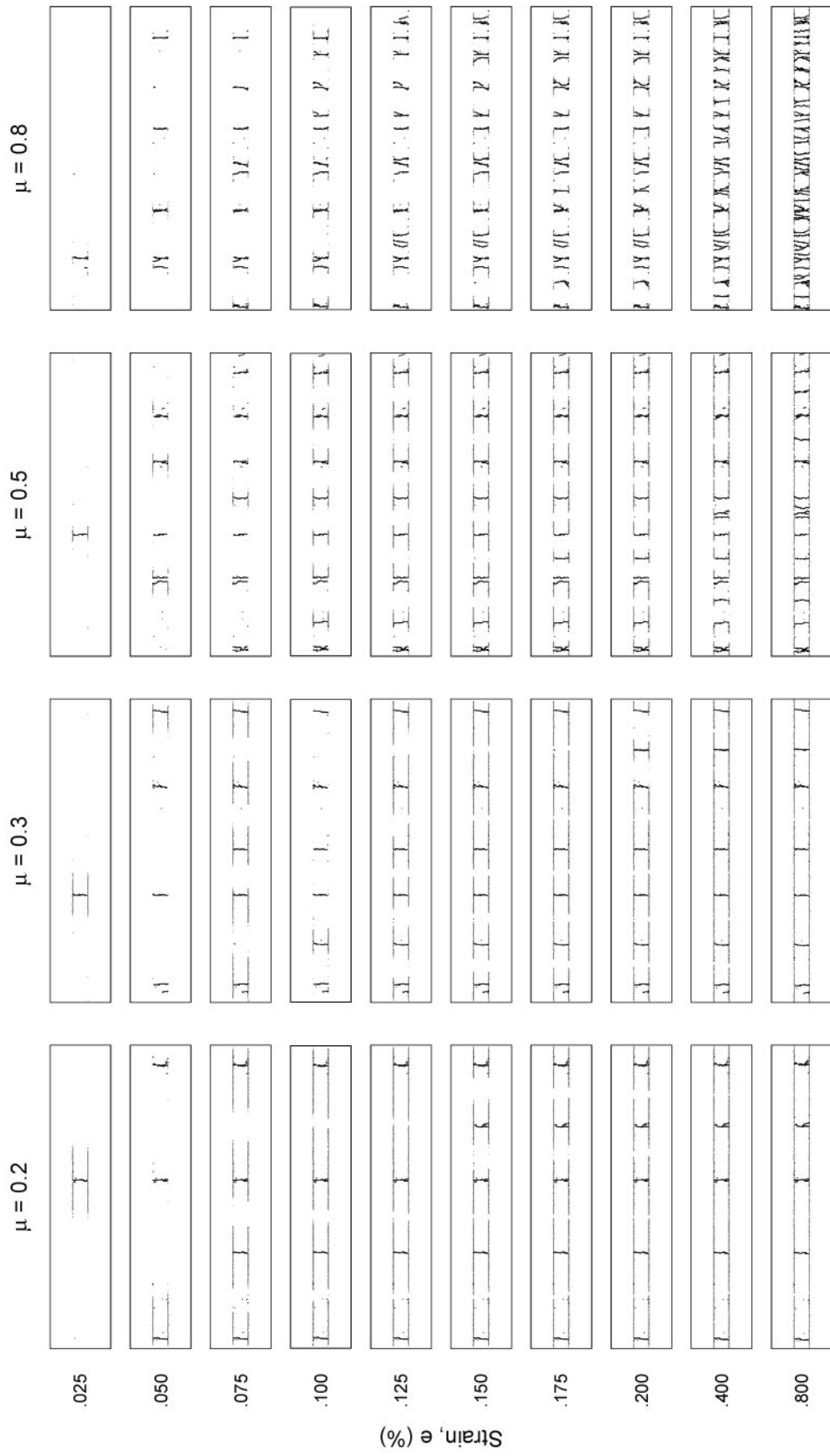


Figure 4: Locations of broken bonds (black) and sliding 'smooth-joint' contacts (grey) at various stages of strain. μ is the interfacial friction coefficient. The frames are 2.0 m wide and 0.4 m high.

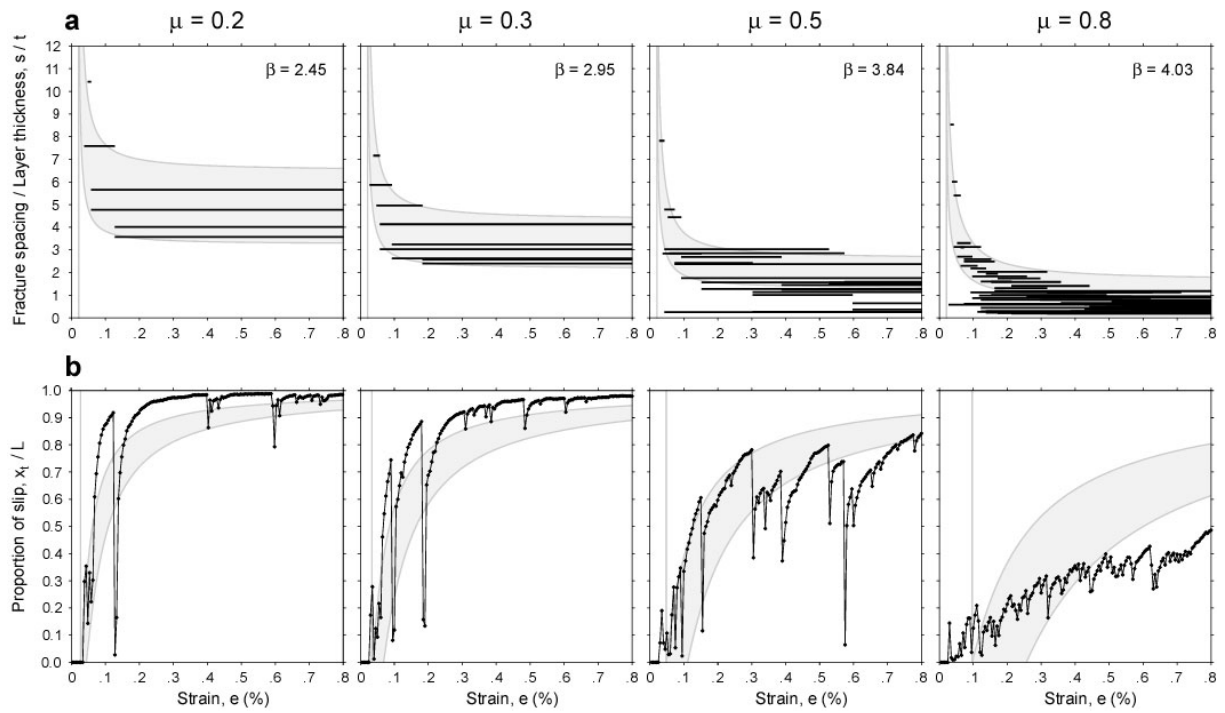


Figure 5: Plots of (a) fracture spacing to layer thickness ratios (black horizontal lines) and (b) average proportions of interfacial slip (black lines with dots) vs. layer parallel strain (e). μ is the interfacial friction coefficient. The start of each horizontal line on the graphs in (a) represents the formation of a fracture bound block within the model; the termination of one line coincides with the formation of two new ones. The grey areas are the ranges predicted by a comparable shear-lag model (see Appendix B and Appendix C). The average best-fit load transfer parameter β is given for each model in (a).

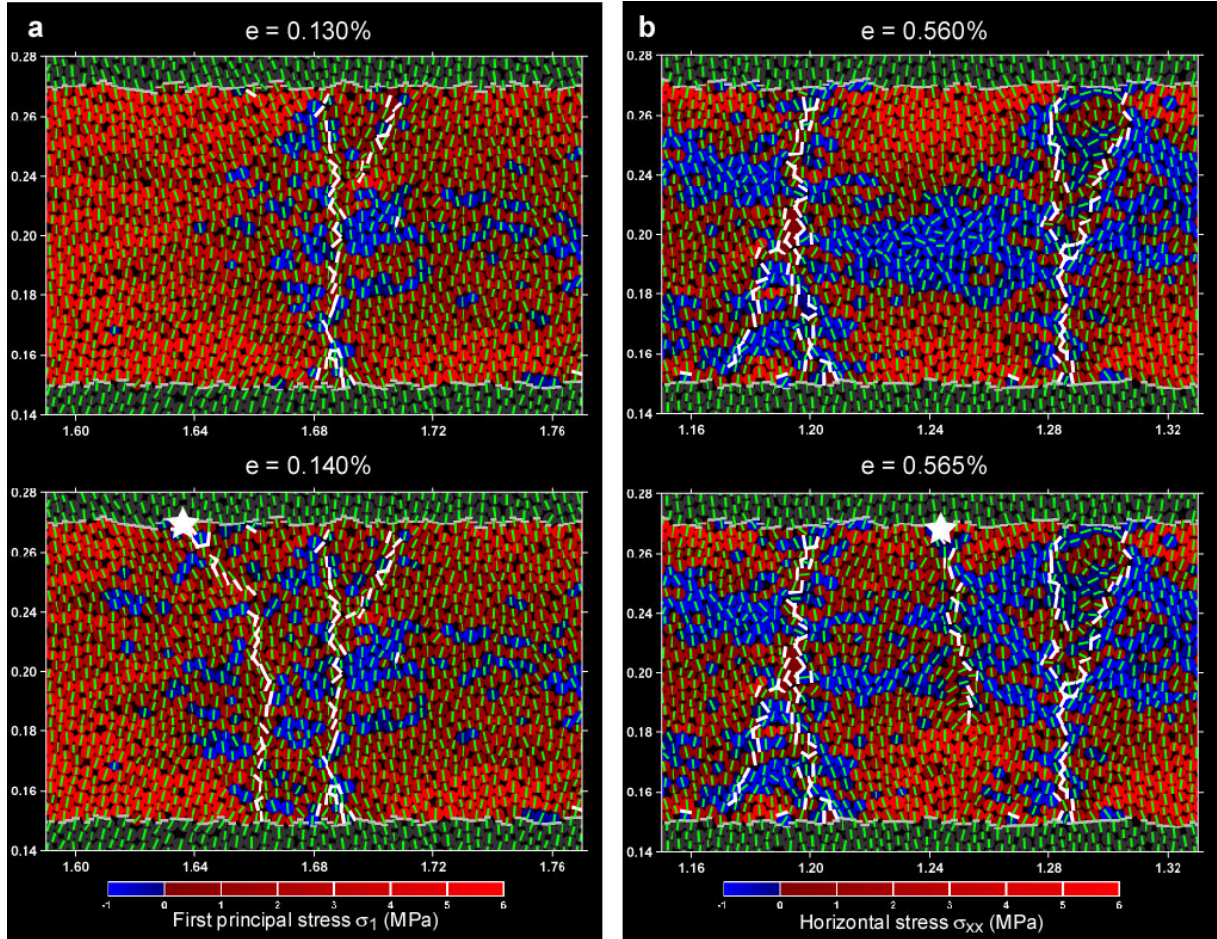


Figure 6: Details of 2-D stress distribution within the high interfacial friction ($\mu = 0.8$) model. **a**, Development of a curved fracture (Groves et al., 1987, Hu et al., 1993) adjacent to an existing straight fracture within a fracture-bound block with a spacing to thickness ratio of ~ 1.9 . **b**, Development of an infill fracture (Bai and Pollard, 2000a) within a fracture-bound block with a spacing to thickness ratio of ~ 0.9 . The infill fracture propagates again at $e = 0.62\%$ to form a through-going fracture (not shown). Particles within the central layer are coloured according to their least compressive stress (σ_1) in **(a)** and according to horizontal normal stress component (σ_{xx}) in **(b)**. Matrix particles are dark grey for clarity. Green lines show direction of minimum, i.e. greatest compressive, principal stress. White and grey lines are locations of broken bonds and ‘smooth joint’ contacts, respectively. Stars are fracture nucleation points. e , model strain.

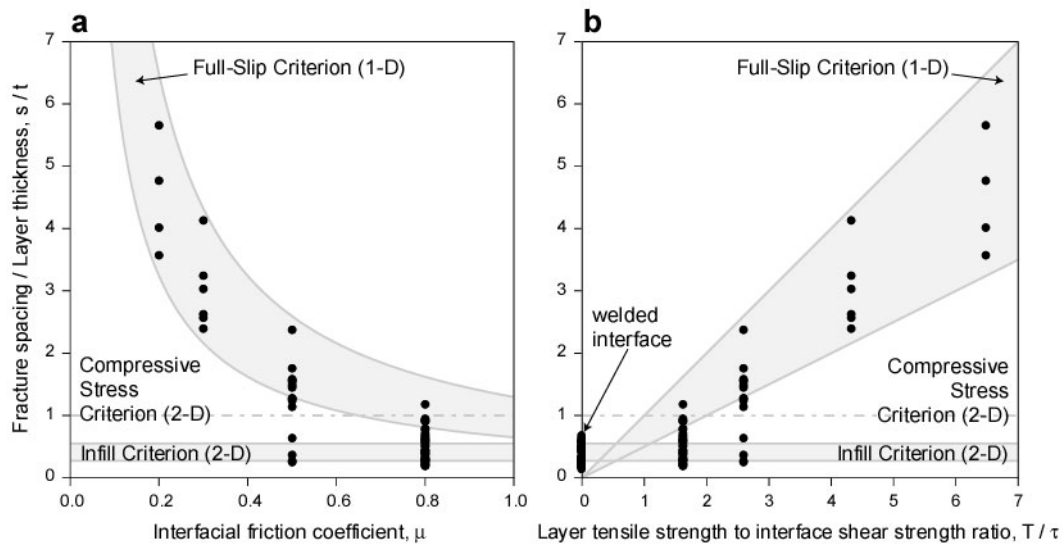


Figure 7: Fracture spacing results at a 'fracture-saturated' model strain of $e = 0.8\%$. Fracture spacing to layer thickness ratio (s/t) is plotted against (a) interfacial friction coefficient μ and (b) layer tensile strength to interface shear strength ratio T/τ . Fracture spacing for a model with a welded interface (i.e. infinite interfacial shear strength) is plotted in (b) only. The grey areas are the ranges predicted by the full-slip (Kelly and Tyson, 1965, Price, 1966) and fracture infill criterion (Bai and Pollard, 2000a). The grey dashed horizontal line at $s/t = 1$ is the theoretical fracture spacing when a central layer-parallel compressive normal stress develops (compressive stress criterion; Bai and Pollard, 2000b).

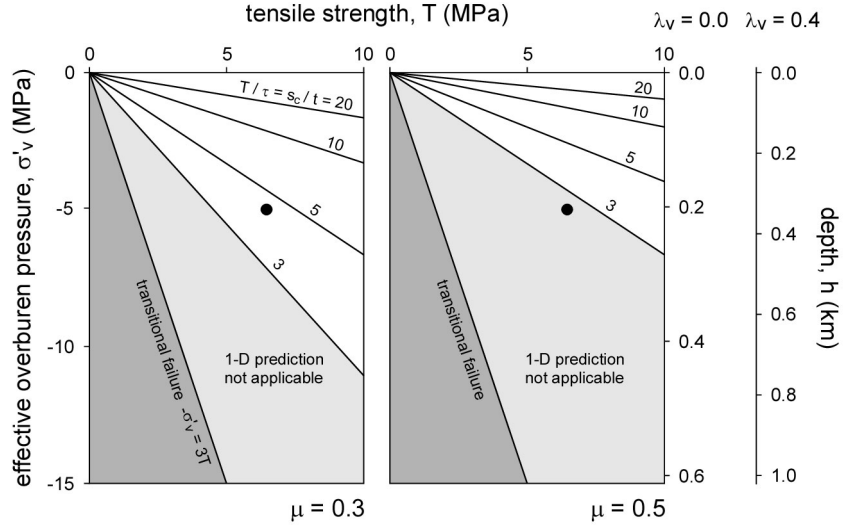


Figure 8: Tensile strength vs effective overburden pressure graphs for interfacial friction coefficients $\mu = 0.3$ and 0.5 illustrating (i) layer tensile to interface shear strength (T/τ) contours (which are equivalent to the ratio of maximum, or critical, fracture spacing to layer thickness under full-slip conditions, s_c/t ; Fig. 1b), (ii) regimes for which our discontinuum models suggest that 1-D full-slip predictions are not applicable ($T/\tau \lesssim 3$; see Fig. 7), and (iii) the transition from pure opening mode fracturing to hybrid extensional-shear fractures, which according to the 2-D Griffith criterion occurs when $-\sigma'_v > 3T$ (e.g. Sibson, 1998). The effective overburden pressure is $\sigma'_v = \sigma_v(1 - \lambda_v)$, with $\lambda_v = p_f/\sigma_v$ being the ratio of pore fluid pressure p_f to vertical stress σ_v . Two depth scales are given, one for lithostatic conditions ($\lambda_v = 0.0$) and one where pore water is present and under normal hydrostatic conditions ($\lambda_v = 0.4$). The dots in each graph illustrate the tensile strength and overburden pressure of our discontinuum models. These graphs are strictly speaking only valid for systems with cohesionless interfaces subjected to layer parallel extension.

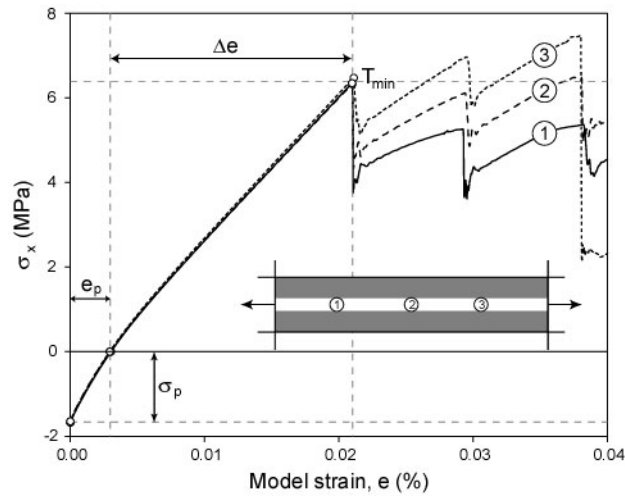


Figure A1: Plot of average horizontal stress within three measurement circles (see inset) vs model strain (for the model with $\mu = 0.3$). After uniaxial model confinement a pre-stress, σ_p exists. The strain at which the horizontal stress within the central layer becomes zero is the pre-strain e_p . T_{min} is the minimum tensile layer strength and Δe is the strain difference used for calculating the layer secant Young's modulus, i.e. $E_f = T_{min}/\Delta e$.

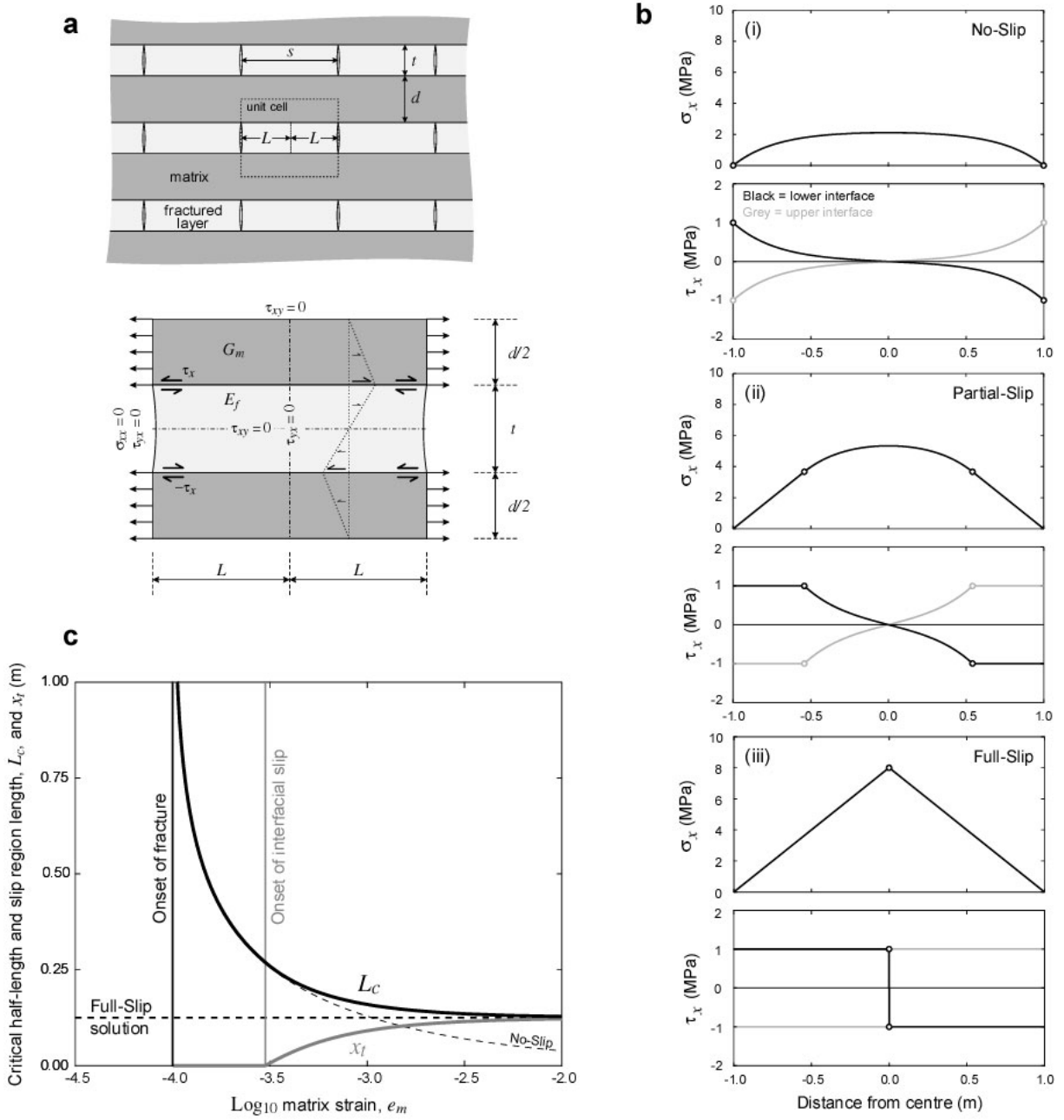


Figure B1: 1-D shear lag model used for predicting fracture and interfacial slip evolution in discontinuum models. **a**, Periodically layered sequence comprised of fractured layers with thickness t interbedded with unfractured matrix layers of thickness d . The spacing of the fractures is s , but due to the symmetry of the problem the half-length L is used. The boundary conditions acting on a 'unit cell' are also shown. **b**, Average horizontal normal stress, σ_x , and interfacial shear stress, τ_x , profiles at different matrix strains, e_m . The dots indicate the transition points from the slip to no-slip region. (i), No-slip solution, just at the onset of slip ($e_m = 0.000224$ according to Eq. B.11) (ii) Partial-slip solution ($e_m = 0.0006$). (iii) Full-slip solution ($e_m = \infty$). **c**, Plot of critical half-length, L_c (black curve), and length of slip region, x_t (grey curve), vs \log_{10} matrix strain, e_m . The onset of fracture and the onset of interfacial slip are indicated as vertical lines. The full-slip solution (Eq. B.14) is plotted as horizontal dashed line. The no-slip solution (Eq. B.10) is plotted as thin dashed line for comparison. The parameters used for obtaining the results in (b) and (c) are: $t = d = 0.25$ m, $E_f = 10$ GPa, $G_m = 1$ GPa, $\tau = 1$ MPa. The β -value is calculated using Eq. B.6. In (b) the half length $L = 1$ m is kept constant, whereas in (c) the tensile strength $T = 1$ MPa is constant.